Supporting Information

Composition- and size-modulated porous bismuth-tin biphase alloys as anodes for advanced magnesium ion batteries

Jiazheng Niu,[1,†] Kuibo Yin,[2,†] Hui Gao,[1] Meijia Song,[1] Wensheng Ma,[1] Zhangquan Peng,[3] Zhonghua Zhang[1,*]

[1]Key Laboratory for Liquid-Solid Structural Evolution and Processing of Materials (Ministry of Education), School of Materials Science and Engineering, Shandong University, Jingshi Road 17923, Jinan, 250061, P.R. China

[2]SEU-FEI Nano-Pico Center, Key Lab of MEMS of Ministry of Education, Southeast University, Nanjing 210096, P.R. China

[3]State Key Laboratory of Electroanalytical Chemistry, Changchun Institute of Applied Chemistry, Chinese Academy of Sciences, Changchun, Jilin 130022, P.R. China

†The authors equally contribute to this work.

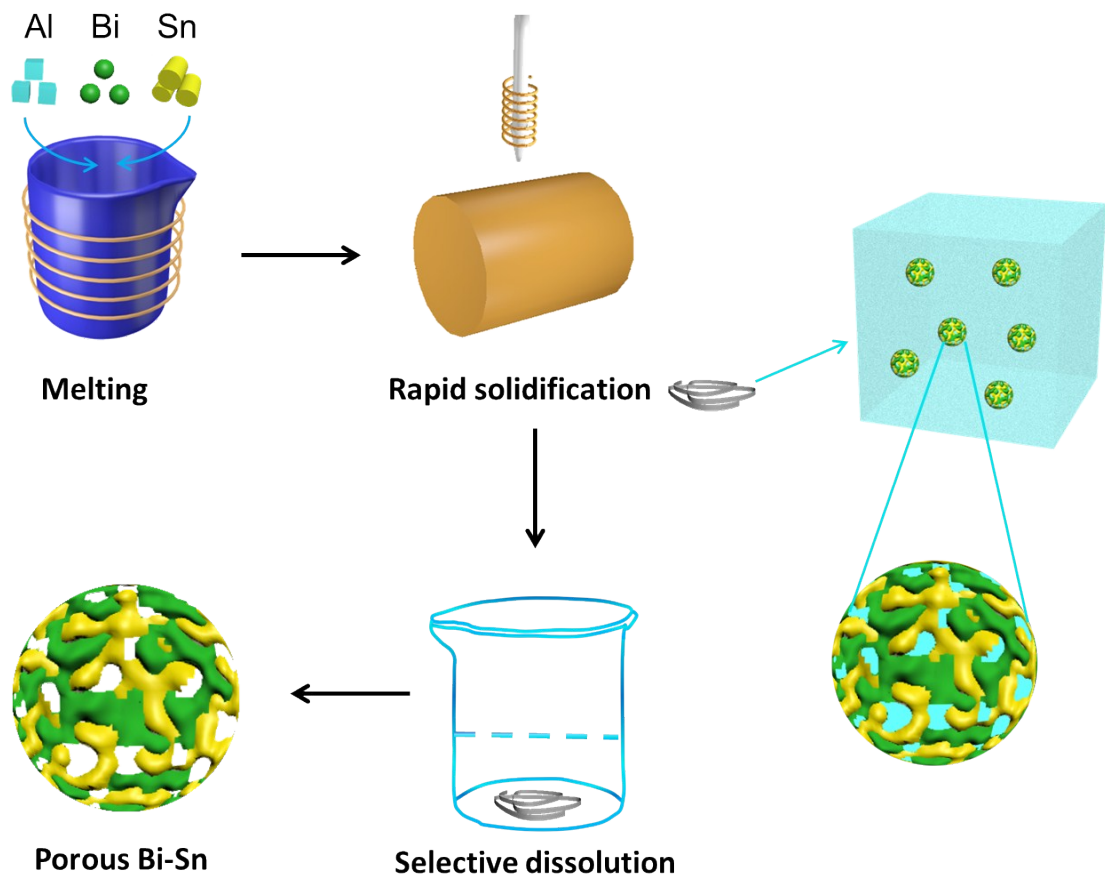*Corresponding author. Email: zh_zhang@sdu.edu.cn (Z. Zhang)

Fig. S1. Schematic illustration of the formation of biphase P-Bi-Sn alloys through selective phase corrosion of rapidly solidified Al-Bi-Sn precursors. The triphase Al-Bi-Sn precursors with different Bi/Sn ratios were designed based upon positive mixing enthalpy between elements of Al, Bi and Sn.
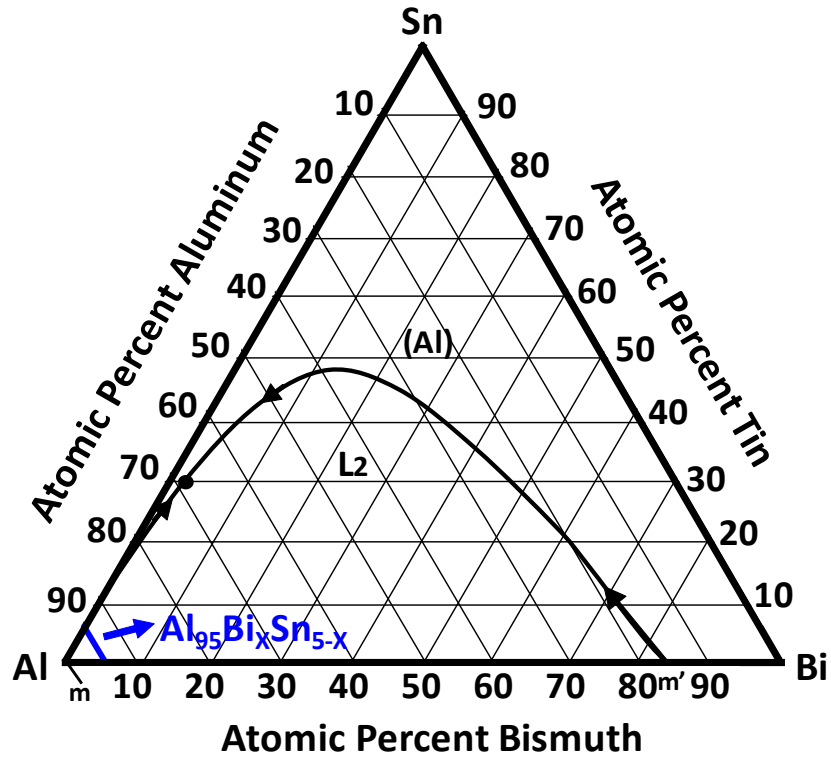
Fig. S2. Al-Bi-Sn phase diagram at 606.6 °C.[1] The compositions of Al-Bi-Sn alloys used in this work are highlighted by a blue line.
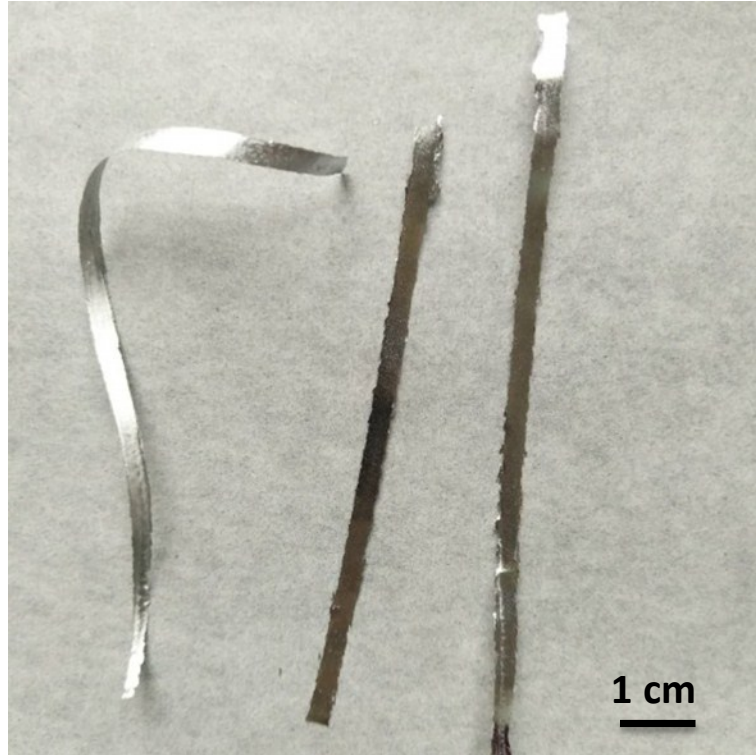
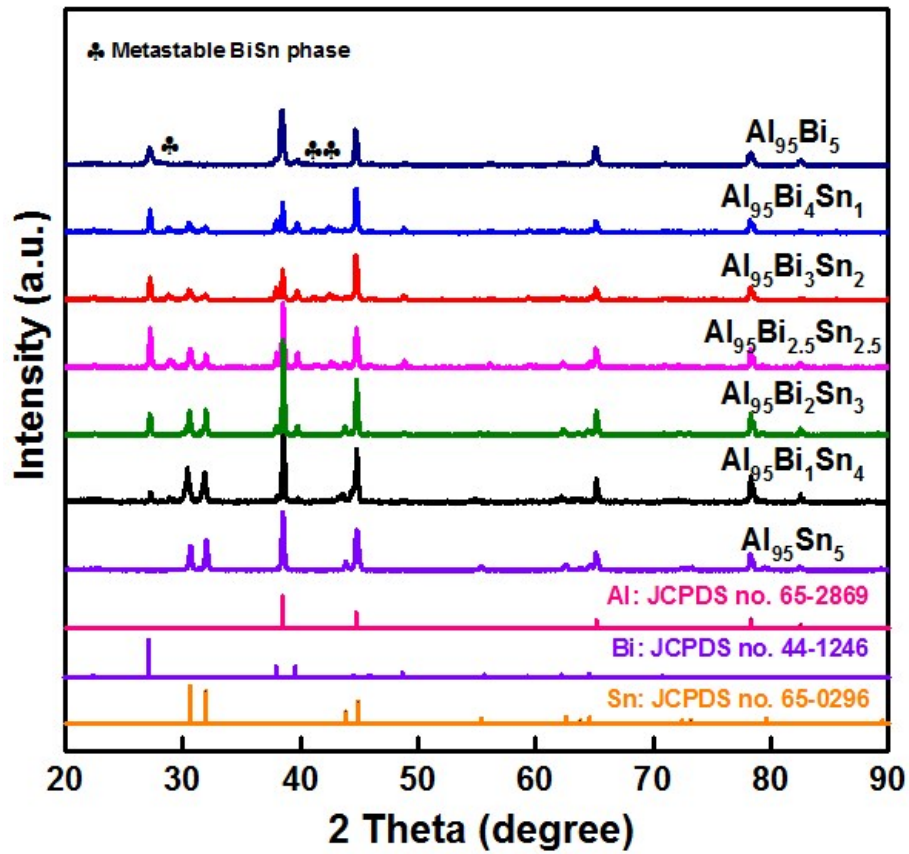Fig. S3. Photograph showing the rapidly solidified Al-Bi-Sn alloy ribbons.

Fig. S4. XRD patterns of the rapidly solidified Al-Bi-Sn precursor alloys. For comparison, the XRD patterns of the rapidly solidified $Al_{95}Bi_5$ and $Al_{95}Sn_5$ are also shown, which are composed of Al/Bi and Al/Sn phases respectively.
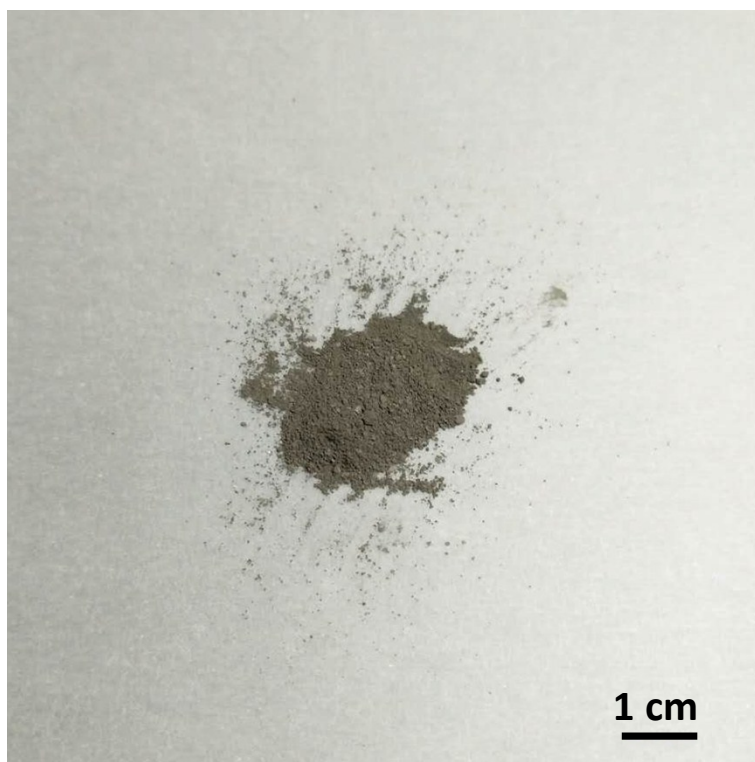
Fig. S5. Photograph obtained after selective phase corrosion showing the final products which are in the form of powders.

Fig. S6. Photograph showing the $Al_{95}Bi_xSn_y$ alloy ingot with a mass of more than 460 g. The present strategy could be easily scaled up.
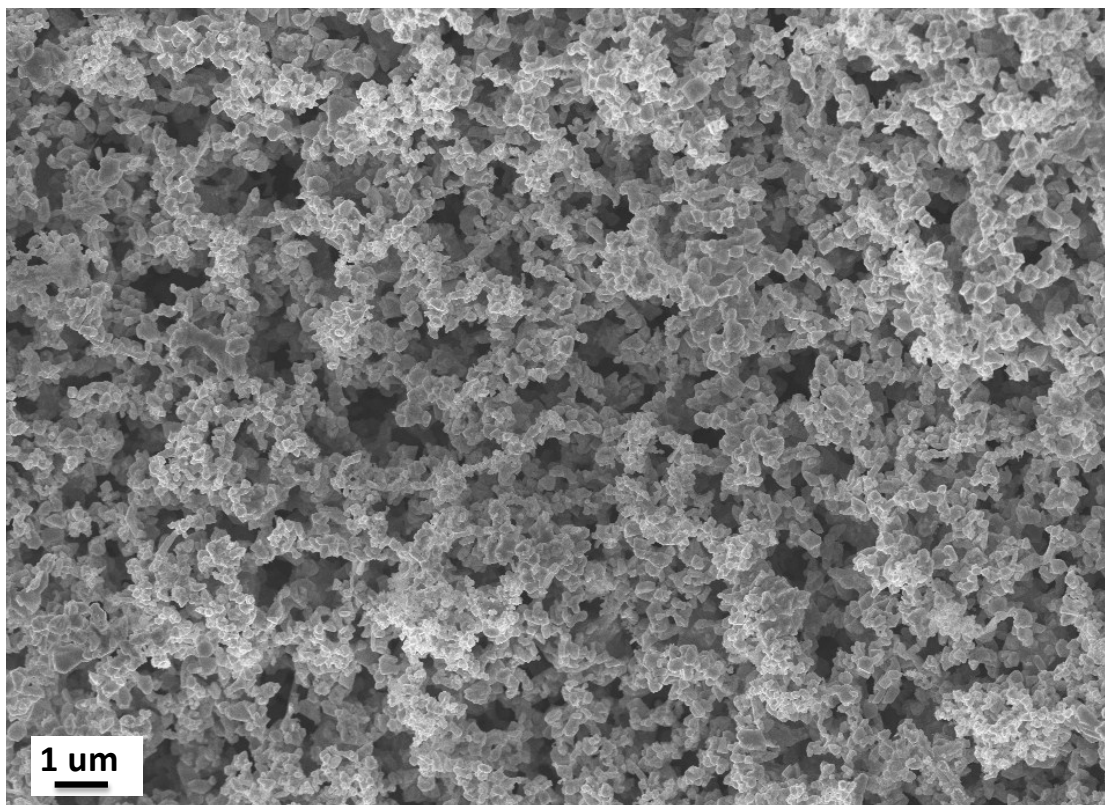
Fig. S7. SEM image at low magnification of P-Bi$_3$Sn$_2$ alloy clearly showing the typical three-dimensional bi-continuous porous architecture.

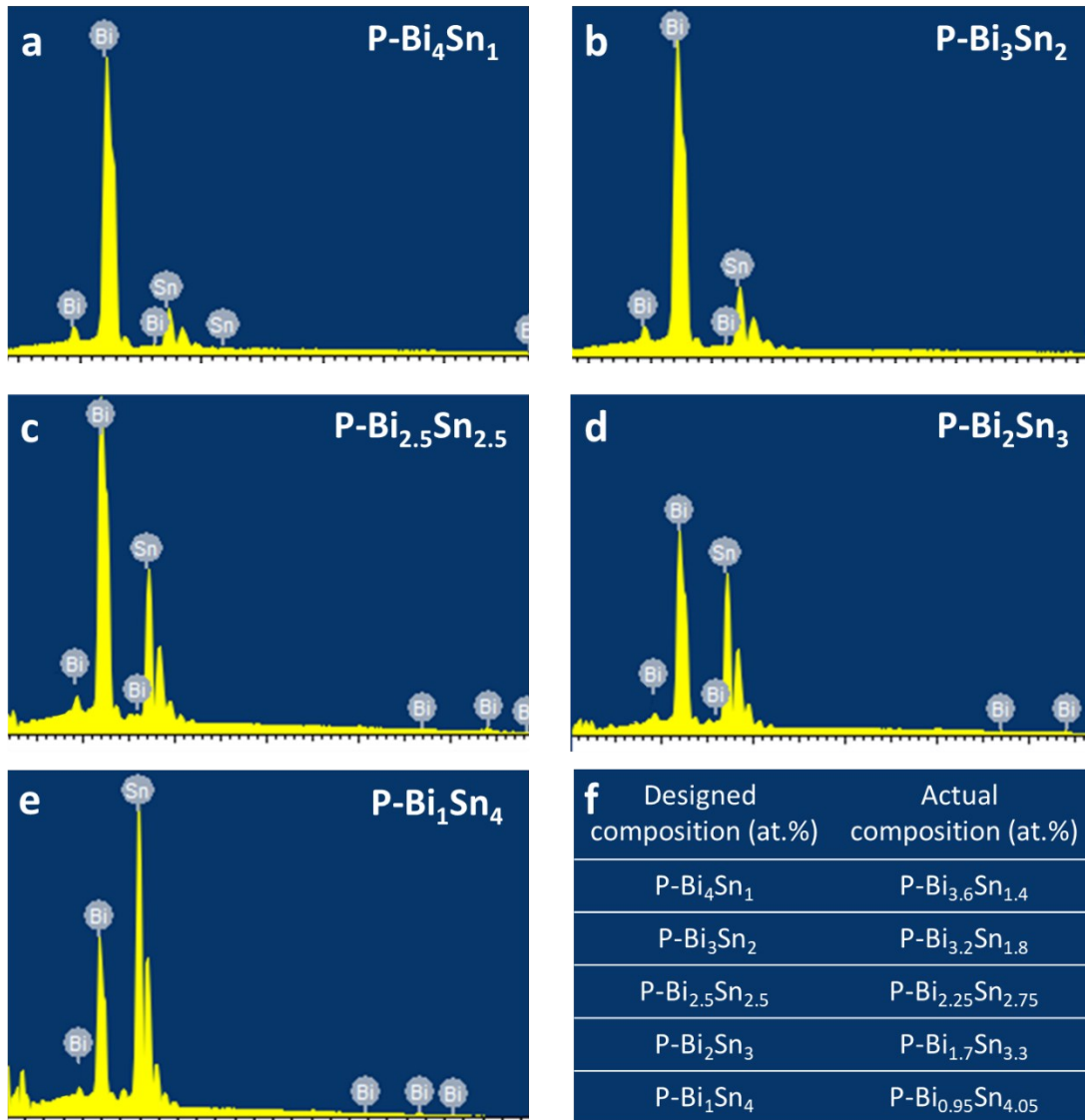| Designed composition (at.%)	Actual composition (at.%)
P-Bi$_4$Sn$_1$	P-Bi$_{3.6}$Sn$_{1.4}$
P-Bi$_3$Sn$_2$	P-Bi$_{3.2}$Sn$_{1.8}$
P-Bi$_{2.5}$Sn$_{2.5}$	P-Bi$_{2.25}$Sn$_{2.75}$
P-Bi$_2$Sn$_3$	P-Bi$_{1.7}$Sn$_{3.3}$
P-Bi$_1$Sn$_4$	P-Bi$_{0.95}$Sn$_{4.05}$

Fig. S8. (a-e) Typical EDX spectrums of biphase P-Bi-Sn alloys. (f) Designed and actual compositions of P-Bi-Sn alloys.
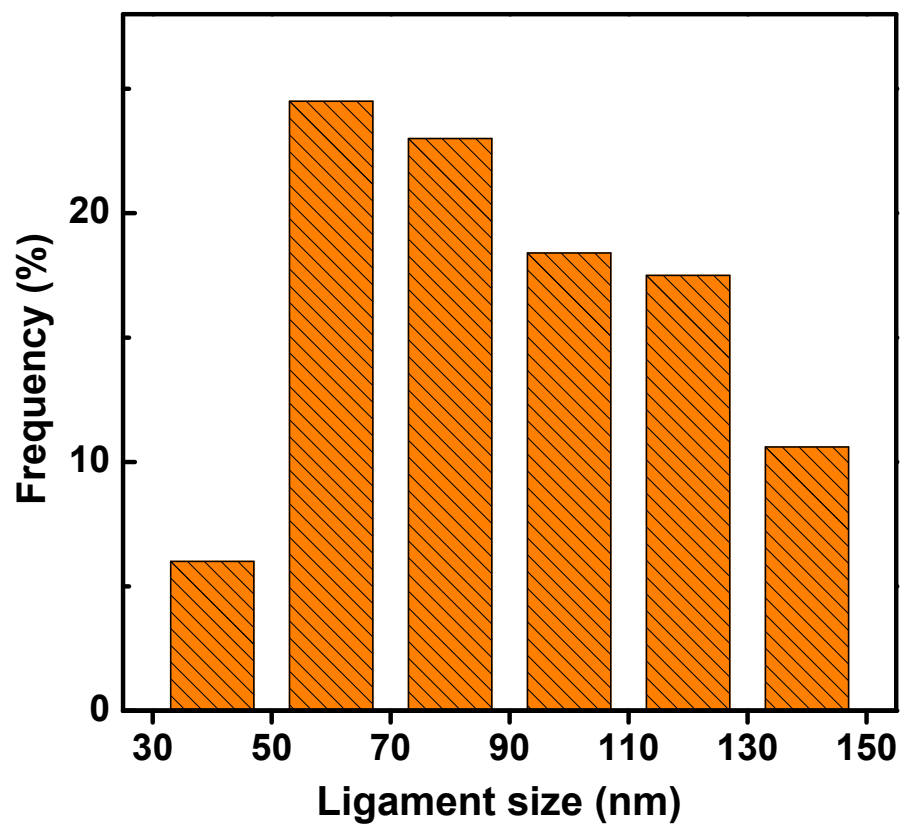
Fig. S9. Ligament size distribution of P-Bi$_3$Sn$_2$ alloy measured from the TEM images.
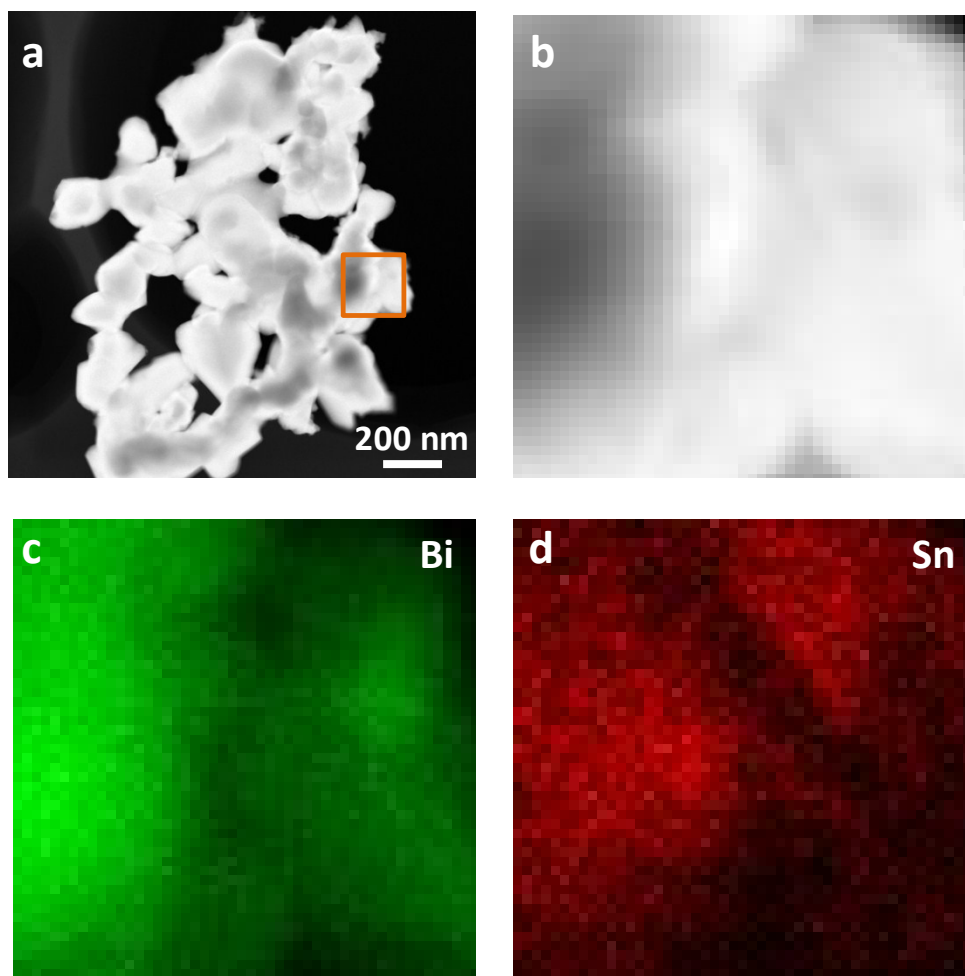
Fig. S10. (a) A HAADF-STEM image of P-Bi$_3$Sn$_2$. The area for EDX mapping is highlighted by an orange box. (b) Simultaneous HAADF-STEM image and (c,d) corresponding EDX mapping spectrums.

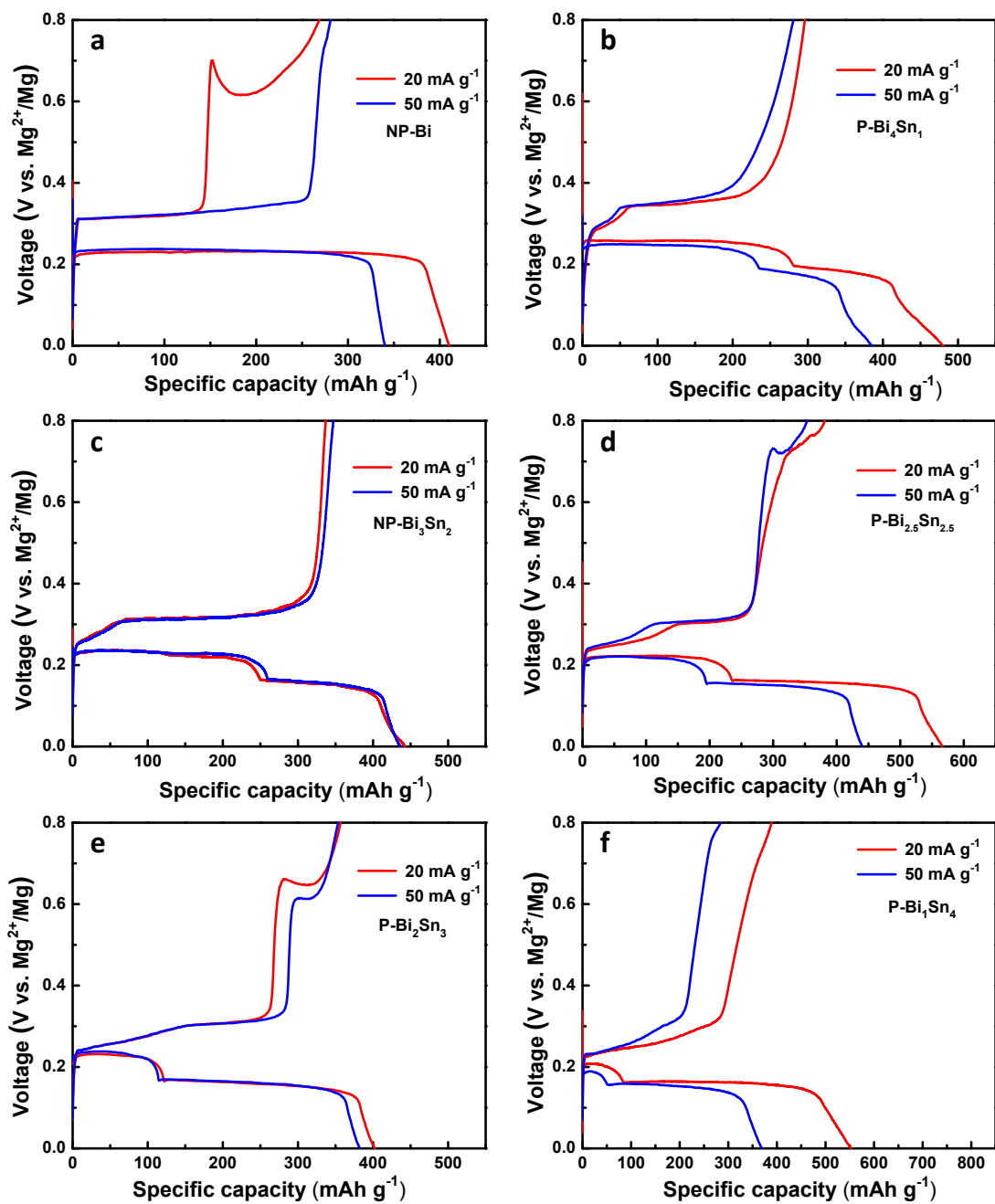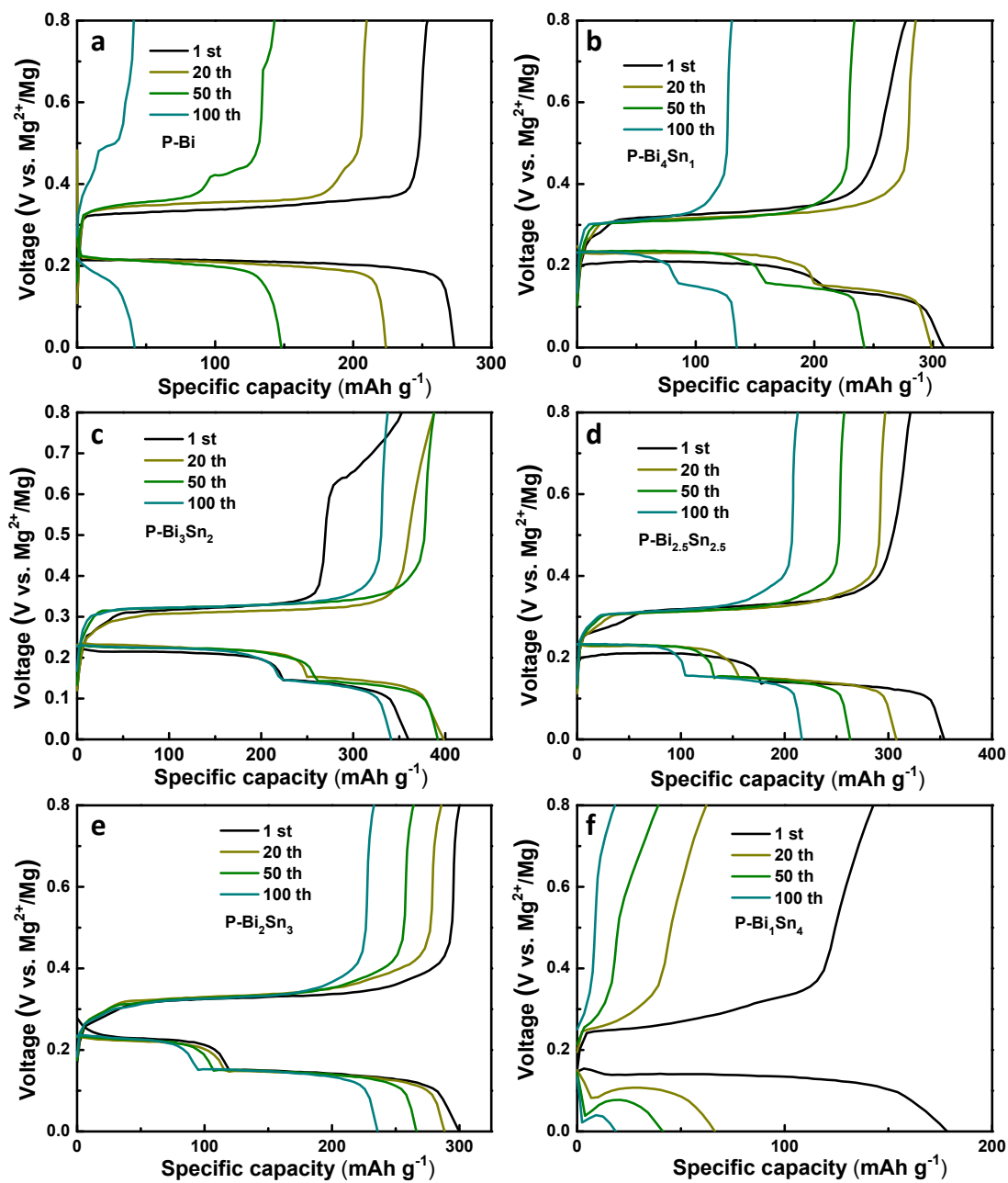Fig. S11. Discharge/charge profiles of P-Bi-Sn and P-Bi electrodes at the current density of 20 and 50 mA g^{-1}.

Fig. S12. Discharge/charge profiles of P-Bi-Sn and P-Bi electrodes in different cycles at the current density of 200 mA g^{-1}.
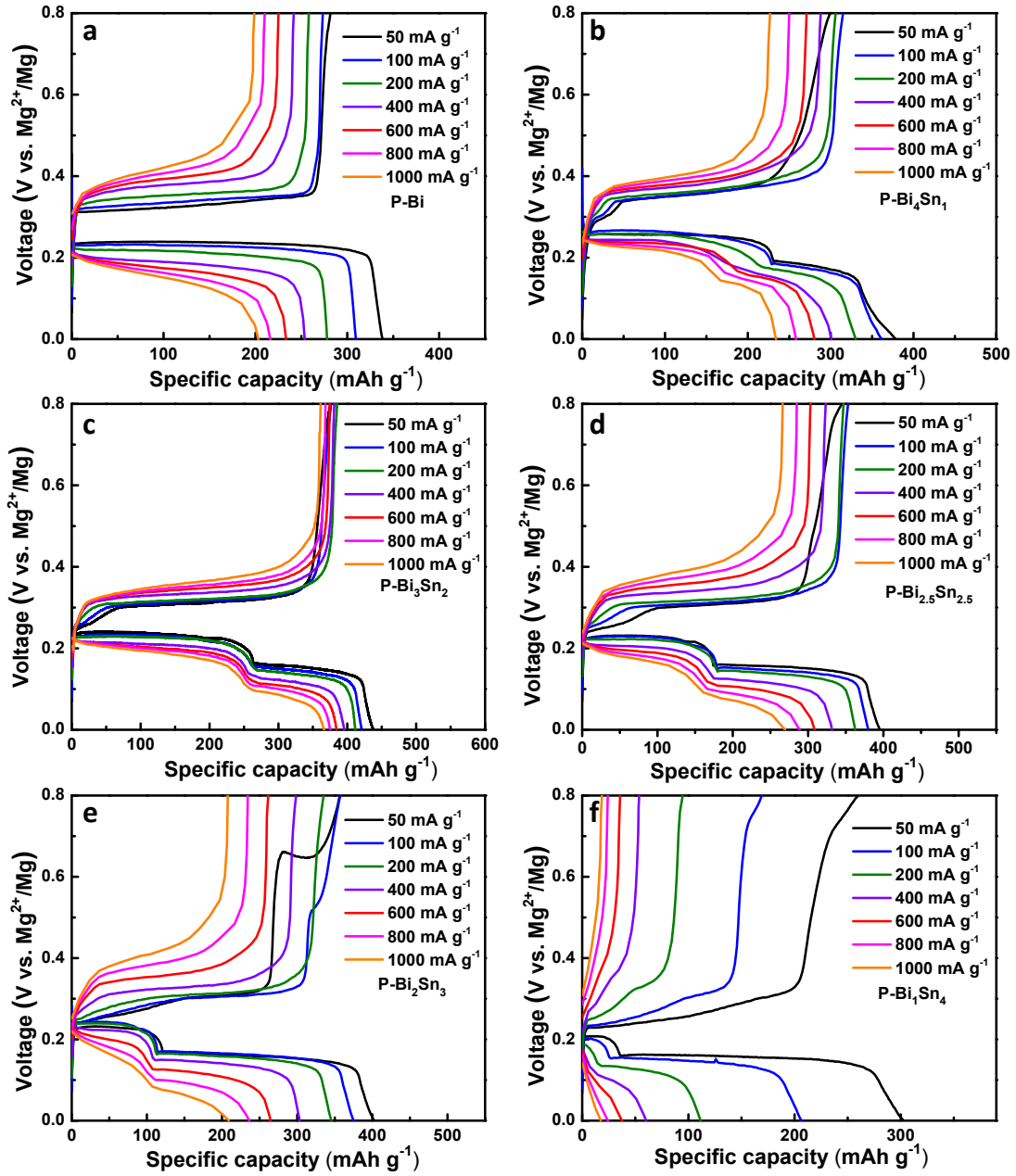
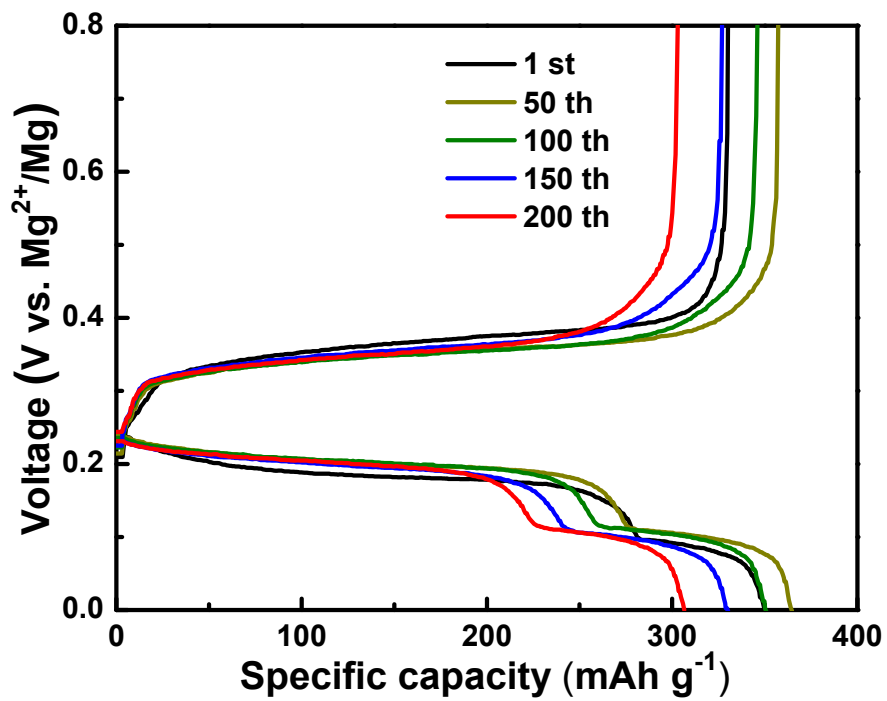Fig. S13. Discharge/charge profiles of P-Bi-Sn and P-Bi electrodes at different current densities from 50 to 1000 mA g^{-1}.

Fig. S14. Discharge/charge profiles of P-Bi$_3$Sn$_2$ electrode in different cycles at the current density of 1000 mA g^{-1}.

References

1. H. X. Liu, C. P. Wang, Y. Yu, X. J. Liu, Y. Takaku, I. Ohnuma, R. Kainuma and K. Ishida, *J. Phase Equilib. Diffus.*, 2012, **33**, 9-19.